



# A NuSTAR and Chandra Investigation of the Misaligned Outflow of PSR J1101–6101 and the Lighthouse Pulsar Wind Nebula

Noel Klingler<sup>1,2,3</sup> , Jeremy Hare<sup>2,7</sup> , Oleg Kargaltsev<sup>4</sup> , George G. Pavlov<sup>5</sup> , and John Tomsick<sup>6</sup>

<sup>1</sup> Center for Space Sciences and Technology, University of Maryland, Baltimore County, Baltimore, MD, 21250, USA

<sup>2</sup> Astrophysics Science Division, NASA Goddard Space Flight Center, Greenbelt, MD, 20771, USA

<sup>3</sup> Center for Research and Exploration in Space Science and Technology, NASA Goddard Space Flight Center, Greenbelt, MD, 20771, USA

<sup>4</sup> Department of Physics, The George Washington University, Washington, DC, 20052, USA

<sup>5</sup> Department of Astronomy & Astrophysics, The Pennsylvania State University, 525 Davey Laboratory, University Park, PA, 16802, USA

<sup>6</sup> Space Sciences Laboratory, University of California, Berkeley, CA, 94720, USA

Received 2022 December 7; revised 2023 April 12; accepted 2023 April 13; published 2023 June 23

## Abstract

PSR J1101–6101 is an energetic young pulsar that powers the remarkable Lighthouse pulsar wind nebula (PWN). The pulsar belongs to the rare type of radio- and gamma-ray-quiet pulsars that are bright in hard X-rays. Moreover, the Lighthouse PWN is remarkable for its misaligned outflow (which gave rise to the PWN’s nickname). Also known as “pulsar filaments,” these collimated parsec-scale X-ray structures have been recently discovered in the vicinity of a handful of fast-moving pulsars, and they appear unaffected by the ram pressure that confines pulsar tails. We report on NuSTAR observations of PSR J1101–6101 and its misaligned outflow—the first observation of such a structure above  $\sim 10$  keV. We detect the outflow up to 25 keV, spatially resolve its spectral evolution with distance from the pulsar, find unambiguous evidence of spectral cooling with distance from the pulsar, and infer physical properties of the particles and magnetic field in the outflow. We also reanalyze archival Chandra data and discuss the outflow’s small-scale structure. We detect pulsations from PSR J1101–6101 up to 20 keV, present the X-ray pulse profile, confirm its period derivative, and perform phase-resolved spectroscopy. Finally, we discuss the X-ray source 2CXO J110158.4–605649 = 2XMM J110158.5–605651 (a serendipitously observed blazar) and suggest it may be the X-ray counterpart to the GeV source 4FGL J1102.0–6054.

*Unified Astronomy Thesaurus concepts:* [Pulsar wind nebulae \(2215\)](#); [Pulsars \(1306\)](#); [X-ray astronomy \(1810\)](#); [Relativistic fluid dynamics \(1389\)](#); [Interstellar medium \(847\)](#); [Interstellar magnetic fields \(845\)](#); [Magnetohydrodynamics \(1964\)](#)

## 1. Introduction

Pulsars are one of nature’s most powerful particle accelerators, capable of accelerating particles up to PeV energies. As a pulsar rotates, it imparts its immense rotational kinetic energy into a magnetized particle wind. As the particles gyrate in the magnetic field, they emit synchrotron radiation (from radio to hard X-rays) and inverse Compton radiation (in the MeV–GeV range), which can be seen as a pulsar wind nebula (PWN; see Kargaltsev et al. 2015; Reynolds et al. 2017 for recent reviews).

Pulsars receive birth kicks during their progenitor supernova explosions, and thus often travel with speeds on the order of hundreds of  $\text{km s}^{-1}$  (Verbunt et al. 2017). If a pulsar moves through the interstellar medium (ISM) with supersonic speed, the ram pressure exerted by the ISM confines the pulsar wind into a parsec-long “tail” behind the moving pulsar (Kargaltsev et al. 2017).

A handful of fast-moving pulsars with observed tails are also accompanied by puzzling parsec-scale X-ray structures strongly misaligned with their pulsars’ directions of motion (see, e.g., Van Etten et al. 2008; Johnson & Wang 2010; Pavan et al. 2014; Klingler et al. 2016a, 2016b; Marelli et al. 2016; de Vries & Romani 2020; Klingler et al. 2020). These so-called

“misaligned outflows” (also referred to as “pulsar filaments”) extend well beyond the extent of the bow shocks and appear to be unaffected by the ram pressure that confines the rest of the pulsar wind. As these structures usually appear to be much brighter and longer on one side, it was proposed that they could be Doppler-boosted pulsar jets along the pulsar spin axis (Pavan et al. 2014); however, deep Chandra X-ray Observatory (CXO) images show that, in at least three such supersonic PWNe (SPWNe), the jets remain confined to the bow shock interior and are unrelated to the misaligned outflows (Klingler et al. 2016a, 2016b).

The parsec-scale sizes, lack of substantial bending, and hard spectra ( $\Gamma = 1.6 - 1.7$ ) exhibited by these outflows (Kargaltsev et al. 2017) led to the suggestion that these structures could occur if high-energy particles escaped into the ISM when the standoff distance at the apex of the bow shock,  $r_s = (\dot{E}/4\pi c \mu m_H n_{\text{ism}} v_{\text{psr}}^2)^{1/2}$ , becomes smaller than the gyroradius of high-energy electrons,  $r_g = \gamma m_e c^2/eB_{\text{pwn}}^{\text{apex}}$  (Bandiera 2008); for pulsar spin-down energy  $\dot{E}$ , hydrogen mass  $m_H$ , average ISM molecular weight  $\mu$ , ISM number density  $n_{\text{ism}}$ , and pulsar velocity  $v_{\text{psr}}$ , Lorentz factor  $\gamma$ ,  $e^\pm$  mass  $m_e$ , and bow shock apex magnetic field  $B_{\text{pwn}}^{\text{apex}}$ . In such a scenario, the escaped wind particles would follow the ambient ISM magnetic field lines (in terms of the bulk flow) and emit synchrotron radiation, therefore illuminating the ISM magnetic field structure.

The detection of a misaligned outflow produced by the transonic PSR J1809–1917 (Klingler et al. 2020) indicated that, in at least some SPWNe, alternative particle escape

<sup>7</sup> NASA Postdoctoral Program Fellow.

Original content from this work may be used under the terms of the [Creative Commons Attribution 4.0 licence](#). Any further distribution of this work must maintain attribution to the author(s) and the title of the work, journal citation and DOI.

mechanisms can occur, as J1809's bow shock standoff distance of 1 pc is incompatible with the compressed bow shock ( $r_s < r_g$ ) explanation. Simulations by Olmi & Bucciantini (2019a, 2019b) suggest that the particle escape can occur due to reconnection of the PWN and ISM magnetic fields in the bow shock (see also Bykov et al. 2017). In this scenario, a magnetic bottle effect at the reconnection region can prevent lower-energy particles from escaping, which can explain why misaligned outflows are not seen in radio even when their accompanying PWNe are (in some cases). Additionally, the opposing helicity of the magnetic fields in each PWN hemisphere causes magnetic reconnection to be favored in the hemisphere whose magnetic field direction opposes that of the ISM, which explains why these outflows are extremely asymmetrical, unlike typical pulsar jets (i.e., polar outflows).

Direct evidence for magnetic interaction is also seen in the Lighthouse PWN. High-resolution Chandra images (see, e.g., Figure 15 of Klingler et al. 2016a) revealed “magnetic draping” (Lyutikov 2006; Dursi & Pfrommer 2008) of the ISM magnetic field (illuminated by the escaped pulsar wind) around the apex of the bow shock. Also, ATCA radio observations (Pavan et al. 2014) showed that none (or very few) of the lower-energy (radio-emitting) pulsar wind particles present in the PWN tail escaped into the outflow, further suggesting a magnetic bottle effect that screens out lower-energy particles.

It has also been proposed that misaligned pulsar outflows are the high-energy analogs of the nonthermal radio filaments seen toward the Galactic center (Barkov & Lyutikov 2019). However, observational evidence directly linking a radio filament and a pulsar misaligned outflow has yet to be seen. In contrast to the misaligned outflows associated with fast-moving pulsars, most of the Galactic center filaments are only detected in radio and not in X-rays (only 4 of the 100+ radio filaments have X-ray counterparts; see, e.g., Zhang et al. 2020; Yusef-Zadeh et al. 2021).

Only a handful of pulsar misaligned outflows are currently known. Their broadband spectral properties remain unknown, as they are not seen in radio and no PWNe of this type have been observed above  $\sim 10$  keV. No substantial evidence of significant spectral cooling with distance from the pulsar has been found in a misaligned outflow so far. The degree of spectral cooling places constraints on particle energies, the particle propagation speed, and magnetic field strength inside the misaligned outflow. This motivated us to obtain hard X-ray observations with NuSTAR of the brightest misaligned outflow, the Lighthouse PWN, powered by PSR J1101–6101, which we report in this paper.

The hard X-ray INTEGRAL source IGR J11014–6103 was first identified as a PWN by Pavan et al. (2011) based on the extended emission seen in X-rays with Swift-XRT and XMM-Newton. Tomsick et al. (2012) proposed an association between this pulsar/PWN and the nearby supernova remnant (SNR) MSH 11–61 A = G290.0–0.8 ( $d = 7 \pm 1$  kpc; Reynoso et al. 2006) based on the pulsar tail morphology and orientation (the tail points back toward the SNR), as resolved with Chandra observations (Figure 1, right panel). This association and the estimated 10–30 kyr age of the SNR (García et al. 2012) imply a very high transverse velocity  $v_{\perp} \sim 800\text{--}2400 \text{ km s}^{-1}$  (among the largest known pulsar velocities; assuming  $d = 7$  kpc). Halpern et al. (2014) detected pulsations with XMM-Newton, revealing PSR J1101–6101 (henceforth J1101) with period  $P = 62.8$  ms, spin-down power  $\dot{E} = 1.6 \times 10^{36} \text{ erg s}^{-1}$ , and

characteristic age  $\tau_c \equiv P/2\dot{P} = 116$  kyr (pulsar parameters are listed in Table 1). The pulsed fraction appears to increase with energy, reaching  $\geq 50\%$  in 4–10 keV. It is worth noting that the association with the G290.0–0.8 SNR implies that the true age of the pulsar must be substantially younger than its characteristic age.

Deep Chandra observations (Pavan et al. 2014, 2016; also see Figure 1, right panel) revealed a hard pulsar spectrum ( $\Gamma_{\text{psr}} = 1.08 \pm 0.08$ ,  $F_{2\text{--}10 \text{ keV}} = 6.2 \times 10^{-13} \text{ erg cm}^{-2} \text{ s}^{-1}$ ), a soft tail with  $\Gamma_{\text{tail}} = 2.22 \pm 0.06$ ,  $F_{2\text{--}10 \text{ keV}} = 6.1 \times 10^{-13} \text{ erg cm}^{-2} \text{ s}^{-1}$  cgs), and a long ( $> 5'$ ) misaligned outflow ( $\Gamma_{\text{mo}} = 1.7 \pm 0.1$ ,  $F_{2\text{--}10 \text{ keV}} = 6.5 \times 10^{-13} \text{ erg cm}^{-2} \text{ s}^{-1}$ ). The spectrum of the outflow appears to exhibit changes on scales  $> 1'$  (Figure 8 in Pavan et al. 2016). The source is seen with INTEGRAL-ISGRI up to 60 keV, but ISGRI cannot resolve the pulsar from the pulsar tail or misaligned outflow. J1101 is also one of only seven pulsars with  $\dot{E} > 10^{36} \text{ erg s}^{-1}$  that are both radio and gamma-ray quiet (i.e., pulsations from these pulsars have only been detected in X-rays).

## 2. Observations and Data Reduction

### 2.1. NuSTAR

NuSTAR (Harrison et al. 2013) observed J1101 on 2020 November 20 for 136 ks (ObsID 30601029002; PI: Klingler). We reprocessed the data using HEASoft v6.29 c (NASA High Energy Astrophysics Science Archive Research Center (Heasarc), 2014) and NuSTAR CALDB v20211202 (see Madsen et al. 2022 for details), which includes the latest calibration updates at the time of analysis/writing. We ran the standard tool, nupipeline, which applied all the latest calibrations and filtering, and we barycenter corrected the arrival times of photons originating from the pulsar's position, using NuSTAR clock correction file 20100101v128, which also corrects for NuSTAR's clock drift, providing a timing accuracy of  $\sim 65 \mu\text{s}$  (Bachetti et al. 2021). We extracted spectra using nuproducts (with option `extended=yes` for analysis of the misaligned outflow).

### 2.2. Chandra

Chandra observed J1101 and its PWN for a total of 286 ks between 2012 October and 2014 October (PI: Pavan), with the ACIS-I detector (time resolution = 3.2 s). We utilized the archival observations (see Table 2) in some of the spectral analyses of extended emission, described in subsequent sections.

We processed the data using the CIAO software package v4.13 and CALDB v4.9.6 (Fruscione et al. 2006). We ran the standard tool chandra\_repro, which applied all the latest calibrations and filtering, and extracted spectra using specextract (with options `weight=yes` and `correctpsf=no` when analyzing regions of extended emission). We restricted the Chandra data to the 0.5–8 keV energy range.

### 2.3. Fermi-LAT

No Fermi-LAT GeV source is reported at the position of PSR J1101 in the 4FGL-DR3 catalog, which was constructed using 12 yr of Fermi-LAT data (Abdollahi et al. 2022). We downloaded the Fermi-LAT data extending up to MJD 59771.6, which includes almost 14 yr of observations, to search for a potential GeV counterpart to PSR J1101 or its

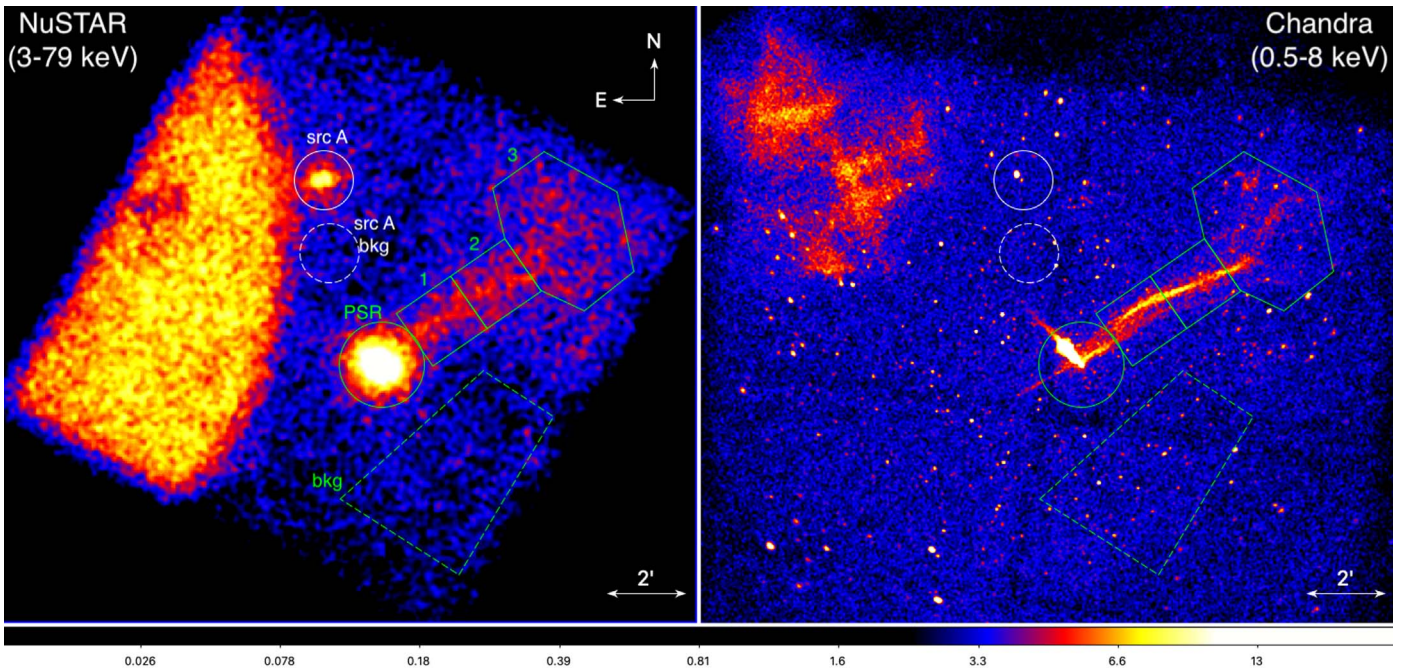


**Figure 1.** Images of the J1101 field and the Lighthouse PWN. Left: NuSTAR (3–79 keV, FPMA+FPMB combined, 136 ks, smoothed with a four-pixel Gaussian kernel). Right: Chandra (ACIS-I, 0.5–8 keV, 286 ks, binned by a factor of two and smoothed with a three-pixel ( $r = 3'$ ) Gaussian kernel). The stray light seen in the eastern part of the NuSTAR image is caused by nearby off-axis source (Cen X-3), and the diffuse emission seen in the northeastern part of the Chandra image is MSH 11–61A (PSR J1101's assumed progenitor SNR). The color bar corresponds to the NuSTAR image and is in units of counts  $\text{pixel}^{-1}$ . The following regions are shown: PSR (green circle); outflow segments 1, 2, and 3 (green boxes/polygon); and source A (white circle). The dashed polygonal region “bkg” was used for background subtraction for analysis of J1101 and the extended emission, and the dashed circle “src A bkg” was used only for analysis of source A (see Section 3.3).

**Table 1**  
Observed and Derived Pulsar Parameters

Parameter	Value
R.A. (J2000.0)	11 01 44.96(9)
Decl. (J2000.0)	-61 01 39.6(7)
Epoch of position (MJD)	56,494
Galactic longitude (deg)	290.040
Galactic latitude (deg)	-0.932
Spin period, $P$ (ms)	62.800077(6)
Period derivative, $\dot{P}$ ( $10^{-15}$ )	8.6(6)
Period epoch (MJD)	56,494
Distance, $d$ (kpc)	$7 \pm 1$
Surface magnetic field, $B_s$ ( $10^{11}$ G)	7.4
Spin-down power, $\dot{E}$ ( $10^{36}$ erg $\text{s}^{-1}$ )	1.4
Spin-down age, $\tau_{\text{sd}} = P/(2\dot{P})$ (kyr)	116

**Note.** Parameters are from the ATNF Pulsar Catalog (Manchester et al. 2005). The distance corresponds to that obtained from H I absorption measurements of SNR MSH 11–61A, by Reynoso et al. (2006).

**Table 2**  
Archival Chandra Observations Used

ObsID	Date	Exposure (ks)
13787	2012 Oct 11	50
16007	2014 Aug 28	116
16517	2014 Sep 5	52
17421	2014 Oct 2	20
17422	2014 Oct 1	49

PWN. The data spanned an energy range of 100 MeV–300 GeV and included a  $15^\circ$  region of interest (ROI) centered on PSR J1101. The data were reduced using the Fermipy

software package (Wood et al. 2017), which uses the latest version (v2.2.0) of Fermi tools. We reduced the data following the standard procedures and used the P8R3\_SOURCE\_V3 version of the response function while selecting the “Source” event class (i.e.,  $\text{evclass} = 128$ ) and using both front and back converting events (i.e.,  $\text{evtype} = 3$ ). We then performed a binned analysis so that the energy dispersion correction could be used.

We first performed a search for a candidate counterpart to PSR J1101. To accomplish this, we used an initial model based on the source parameters from the 4FGL–DR3 catalog (Abdollahi et al. 2022). The Galactic diffuse emission and isotropic emission were accounted for using the `gll_iem_v07.fits` and `iso_P8R3_SOURCE_V3_v1` models, respectively. We then freed the normalizations for all sources within 3 degrees of PSR J1101’s position, and we also allowed the normalization and photon index of the Galactic diffuse component to vary, as well as the normalization of the isotropic diffuse emission. Once the fit converged, we constructed a TS map of the region, assuming a power-law spectral model with a photon index of 2 for the test source, but no new source was found at the position of PSR J1101. We then derived the  $2\sigma$  upper limits on the Fermi-LAT flux of PSR J1101 from 0.3–3 to 3–30 GeV, assuming a power-law spectral model with a photon index of 2:  $6.6 \times 10^{-13}$  and  $4.4 \times 10^{-13}$  erg  $\text{cm}^{-2} \text{s}^{-1}$ .

### 3. Results

#### 3.1. Misaligned Outflow

For the first time, we detected and resolved a pulsar misaligned outflow above  $\sim 10$  keV (i.e., above the Chandra and *XMM* bands); we present the 3–79 keV image in Figure 1.

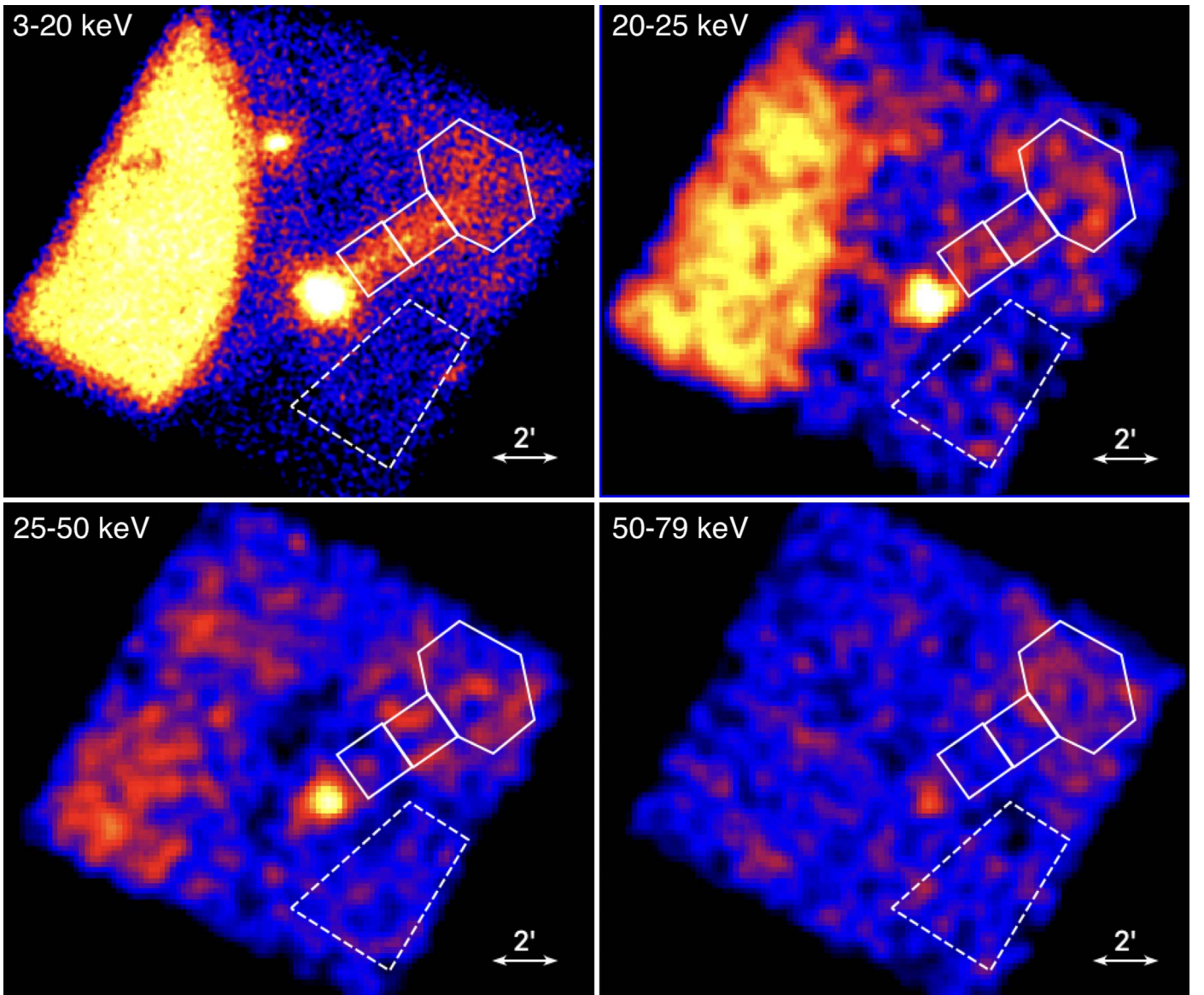


**Figure 2.** NuSTAR images of the Lighthouse PWN in the 3–20 keV, 20–25 keV, 25–50 keV, and 50–79 keV bands (all images are smoothed with a three-pixel Gaussian kernel). The images of the latter three energy bands are binned by a factor of four, for visual clarity.

The outflow can be seen clearly and fully in the NuSTAR images up to energies  $\sim 25$  keV. Surprisingly, traces of segment 3 of the outflow can be faintly seen in the 50–79 keV band (Figure 2). However, this is likely due to elevated background emission in this vicinity (as is seen by the lower-quality spectral fit to segment 3 compared to the other two; see below). The outflow is visible up to a distance of  $\sim 7.5'$  from the pulsar; this is limited by the NuSTAR (and Chandra) FOV, so the outflow's actual extent may be longer. The outflow's size and shape are comparable to those seen in the Chandra images, although the NuSTAR image is substantially blurred due to NuSTAR's broader PSF. In the NuSTAR image, we also see the outflow start to broaden and decollimate about  $5'$  away from the pulsar, as is also seen in the Chandra image.

We extracted the outflow's spatially resolved spectra using three different regions, shown by the green boxes and the polygon in Figure 1. We used a background region located ahead of the moving pulsar (i.e., southwest of it) to minimize

contamination by PWN emission. We binned the spectra using `ftgrouppha` and required a minimum S/N = 6 for each bin. We fit the NuSTAR outflow spectra with an absorbed power-law (PL) model (XSPEC's `tbabs`, which utilizes the abundances of Wilms et al. 2000). The absorbing hydrogen column density was fixed to  $N_{\text{H}} = 0.99 \times 10^{22} \text{ cm}^{-2}$ , which is the best-fit value found by Pavan et al. (2016) while fitting both the pulsar tail and the outflow (independently) using Chandra data. The model was multiplied by a constant that was set to 1.0 for the FPMA data and left as a free parameter for the FPMB data, in order to account for differing sensitivities between the two detectors.

We show the fitted spectra in Figure 3 and list the fit parameters in Table 3. Moving along the outflow (away from the pulsar), we found significant spectral evolution with distance from the pulsar, with the spectral slope changing from  $\Gamma_1 = 1.79 \pm 0.08$  to  $\Gamma_3 = 2.21 \pm 0.08$  (between segments 1 and 3, respectively; 3–79 keV). To verify that our results were not skewed by the higher-energy bins (in which the source count rates become progressively lower and the background becomes increasingly higher), we

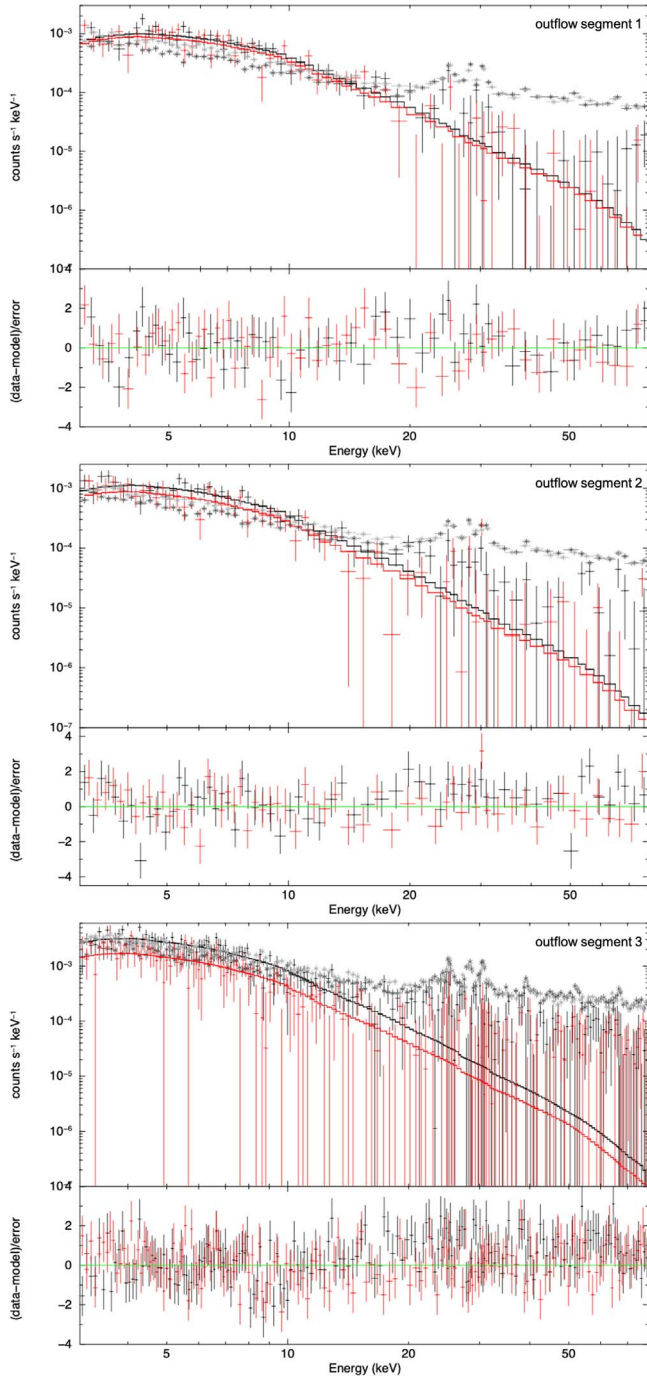


**Figure 3.** Spectral fits of the three outflow segments to the NuSTAR data, binned by a minimum S/N = 6. The black and red data points show the FPMA and FPMB data, respectively, and the corresponding background is shown by the starred dark and light gray data points. As mentioned in the text, restricting the fits to the 3–20 keV range does not noticeably change the best-fit spectral parameters.

restricted the NuSTAR fits to the 3–20 keV range. We obtained  $\Gamma_1 = 1.81 \pm 0.08$ ,  $\Gamma_2 = 2.08 \pm 0.09$ , and  $\Gamma_3 = 2.31 \pm 0.08$ ; thus, these results were consistent with the previous (3–79 keV) results. We note that the fit quality spectrum of segment 3 (reduced  $\chi^2_{348} = 1.21$ ) is slightly worse than that of segments 1 and 2 (reduced  $\chi^2_{122} = 1.04$  and  $\chi^2_{122} = 1.12$ , respectively), which is likely due to the elevated background in the segment 3 vicinity (see the bottom right panel of Figure 2).

For a comparison, we also extracted and fit the spectra of the three outflow segments from the Chandra data (0.5–8 keV). We excluded all point sources present in the source and background regions, and we binned the spectra by requiring S/N = 4 for each bin; the results are listed in Table 4. For segment 1, the spectra are compatible:  $\Gamma_{1,\text{CXO}} = 1.71 \pm 0.04$  and  $\Gamma_{1,\text{Nu}} = 1.79 \pm 0.08$ . However, in the subsequent segments, the differences become prominent:  $\Gamma_{2,\text{CXO}} = 1.86 \pm 0.05$  versus  $\Gamma_{2,\text{Nu}} = 2.03 \pm 0.09$ , and  $\Gamma_{3,\text{CXO}} = 1.74 \pm 0.05$  versus  $\Gamma_{3,\text{Nu}} = 2.21 \pm 0.08$ . Thus, the Chandra spectra do not show consistent spectral cooling with distance, contrary to the NuSTAR data. This might suggest that the effects of spectral cooling in the outflow are only noticeably seen at higher energies.

As similar differences were also seen in the comparison of Chandra and NuSTAR data in studies of the high-mass X-ray/gamma-ray binary LS 5039 (Volkov et al. 2021) and PSR J1617–5055 (Hare et al. 2021), they are likely due to calibration uncertainties (see also Madsen et al. 2017). Therefore, joint Chandra+NuSTAR fits of the Lighthouse data are not warranted here.

Finally, we fitted the Chandra and NuSTAR data in the 3–10 keV band (separately). For Chandra, we obtained  $\Gamma_1 = 1.70 \pm 0.15$ ,  $\Gamma_2 = 2.07 \pm 0.19$ , and  $\Gamma_3 = 2.16 \pm 0.19$  (however, in the Chandra data, most of the spectral bins above 6–7 keV have lower limits consistent with 0 net counts). For NuSTAR, we obtained  $\Gamma_1 = 1.87 \pm 0.13$ ,  $\Gamma_2 = 2.15 \pm 0.13$ , and  $\Gamma_3 = 2.44 \pm 0.10$ . These results again indicate that only the higher-energy part of the spectrum (e.g., >3 keV) shows noticeable signs of spectral cooling.

### 3.2. Pulsar

#### 3.2.1. Timing

Up until recently, J1101 had no long-term timing solution, as it is neither a radio nor a gamma-ray pulsar. However, Ho et al. (2022) used NICER monitoring to obtain an updated timing solution for J1101, which overlaps with the epoch of the NuSTAR observation. This timing solution was published shortly before the conclusion of this work, so we used the pulse period that we found in the NuSTAR data to create phase-folded light curves and phase-resolved spectra. To investigate the dependence of the pulse profile on energy, we used only the NuSTAR data. To find the spin period and its uncertainty, we used the  $Z_1^2$  test (Buccheri et al. 1983). Given that NuSTAR cannot resolve the extended PWN from the point-like pulsar, we searched over different source extraction aperture radii and photon energies to maximize the signal. We found that an extraction radius of 60'' ( $\approx 75\%$  PSF) and photons in the 3–40 keV energy range give the maximum  $Z_1^2$ .

After applying the optimal energy and source extraction radius cuts, we found a  $Z_1^2 = 208.6$  peak at a frequency of  $f = 15.92303947(15)$  Hz. To estimate the  $1\sigma$  uncertainty on the frequency, we use  $\sigma_f = (\sqrt{3}/\pi)T_{\text{span}}^{-1}(Z_{1,\text{max}}^2)^{-1/2}$ , which is valid when the pulsations are purely sinusoidal (i.e.,  $m = 1$ ) and there are no gaps in the time series (see, e.g., Hare et al. 2021). Of course, the J1101 time series has gaps due to the source being occulted by the Earth throughout NuSTAR's orbit, so this formula only provides an estimate on the uncertainty. We find that this timing solution at the epoch  $t_0 = 59175.34321456$  MJD is consistent within uncertainties with the timing solution recently reported by Ho et al. (2022).

**Table 3**  
Misaligned Outflow NuSTAR Spectra

Segment	Area	Net Counts	$\Gamma$	$N_{-5}$	Constant	$\chi^2_\nu$ (dof)	$F_{-13}$	$L_{33}$
1	9650	$1838 \pm 74$	$1.79 \pm 0.08$	$7.6 \pm 1.2$	$0.90 \pm 0.06$	1.04 (122)	$7.1 \pm 0.5$	$4.2 \pm 0.3$
2	9660	$1863 \pm 74$	$2.03 \pm 0.09$	$13.1 \pm 2.2$	$0.81 \pm 0.06$	1.12 (122)	$6.3 \pm 0.6$	$3.7 \pm 0.4$
3	33,180	$4293 \pm 147$	$2.21 \pm 0.08$	$64.3 \pm 9.5$	$0.59 \pm 0.04$	1.21 (348)	$18.7 \pm 1.0$	$11.3 \pm 0.6$

**Note.** Spectral fit results for the misaligned outflow using NuSTAR data (3–79 keV). Listed are the segment number, area (in units of arcsec<sup>2</sup>), net counts, photon index  $\Gamma$ , PL normalization (in units of  $10^{-5}$  photons s<sup>-1</sup> cm<sup>-2</sup> keV<sup>-1</sup> at 1 keV), constant (fit to the FPMB data), reduced  $\chi^2_\nu$  ( $\nu$  degrees of freedom), observed (absorbed) 3–79 keV flux (in units of  $10^{-13}$  erg cm<sup>-2</sup> s<sup>-1</sup>), and luminosity (in units of  $10^{33}$  erg s<sup>-1</sup>, assuming  $d = 7$  kpc). In all fits, we set  $N_{\text{H}} = 0.99 \times 10^{22}$  cm<sup>-2</sup>.

We present the 3–40 keV pulse profile for J1101 in Figure 4. The pulse profile shows a single wide pulse with a relatively broad flat top without a sharp peak. As previously mentioned, NuSTAR cannot resolve the pulsar from the PWN and the part of the outflow in the pulsar’s vicinity, which makes it difficult to accurately estimate the pulsed fraction (or explore its dependence on energy), as we do not reliably know the contribution from those structures. Modeling the contribution from the tail and misaligned outflow using spectra extracted from the Chandra data would not yield reliable results, due to the fact that the same regions exhibit different spectra in the Chandra and NuSTAR data, due to the calibration uncertainties, as demonstrated above in Section 3.1.

### 3.2.2. Phase-integrated Spectroscopy

We first performed fits to the phase-integrated pulsar spectra. To do this, we extract the spectra from an  $r = 30''$  circular region centered on the pulsar. NuSTAR is unable to resolve the pulsar from the PWN, which has an extent of  $\sim 30''$  for the brightest part (see Figure 2 in Pavan et al. 2016), but the PWN can be roughly modeled when modeling the pulsar’s spectrum. Modeling the spectrum of the misaligned outflow is much more difficult, as it is unclear what fraction of the outflow is contained in a given region. Therefore, this extraction region was chosen to minimize the impact of the contamination of the emission from the base of the misaligned outflow on the pulsar’s spectrum. The background was extracted from a source-free region offset from the pulsar, PWN, and misaligned outflow. Prior to fitting, the spectra were binned to have a signal-to-noise ratio of at least 5 per bin. The spectra from the two focal plane modules (FPMA and FPMB) were simultaneously fit, and we use a `const` parameter to account for calibration uncertainties between the two detectors. We find that the difference between normalizations remains  $< 5\%$  throughout all fits of the pulsar+PWN spectra.

We fit the spectra with an absorbed power-law model. The absorbing column density was frozen to the same value used to fit the misaligned outflow (i.e.,  $N_{\text{H}} = 0.99 \times 10^{22}$  cm<sup>-2</sup>; see Section 3.1). We find a photon index  $\Gamma = 1.48 \pm 0.03$ , an unabsorbed 3–79 keV flux of  $(5.2 \pm 0.2) \times 10^{-12}$  erg cm<sup>-2</sup> s<sup>-1</sup>, and  $\chi^2 = 148$  for 149 degrees of freedom (dof). This photon index is larger than previously found by Pavan et al. (2016) for the pulsar using Chandra data ( $\Gamma_{\text{CXO}} = 1.08 \pm 0.08$ ), most likely due to the PWN, which was not accounted for in our fits. To account for this PWN emission, we use the results of the spatially resolved spectral fits performed by Pavan et al. (2016). To accomplish this, we included the anticipated contribution of the PWN as an additional power-law component in the model, freezing the flux and photon index to the values of  $\Gamma = 2.22 \pm 0.06$  and  $F_{2-10 \text{ keV}} = 6.1 \times 10^{-13}$  erg cm<sup>-2</sup> s<sup>-1</sup> found by Pavan et al. (2016). After accounting for the

PWN emission, we find that the pulsar’s fitted photon index decreases to  $\Gamma = 1.14 \pm 0.04$  and the unabsorbed 3–79 keV flux remains virtually the same:  $(4.9 \pm 0.3) \times 10^{-12}$  erg cm<sup>-2</sup> s<sup>-1</sup>, with  $\chi^2 = 146$  for 149 d.o.f. The pulsar’s flux in the 2–10 keV band,  $F_{2-10 \text{ keV}} = (6.6 \pm 0.3) \times 10^{-13}$  erg cm<sup>-2</sup> s<sup>-1</sup> is comparable to that found by Pavan et al. (2016).

We also tried a larger region (i.e.,  $r = 50''$ ) to increase the statistics and better constrain the photon index. However, we found that, after accounting for the PWN emission, the photon index becomes much larger ( $\Gamma = 1.31 \pm 0.03$ ), and the flux,  $F_{2-10 \text{ keV}} = (9.2 \pm 0.3) \times 10^{-13}$  erg cm<sup>-2</sup> s<sup>-1</sup>, increases, becoming incompatible with the pulsar flux reported by Pavan et al. (2016). This increase in flux and the larger photon index are likely due to the additional contribution from the base of the misaligned outflow contaminating the pulsar+PWN spectrum. This further supports the choice of a smaller spectral extraction region.

### 3.2.3. Phase-resolved Spectroscopy

In addition to the phase-integrated spectral fits, we have also attempted phase-resolved spectroscopy. The spectra were extracted from the same regions discussed in Section 3.2.2, and the absorbing column density was frozen to the same value. We chose two phase bins corresponding to the pulse maximum (from  $0 < \phi_{\text{max}} < 0.15$  to  $0.7 < \phi_{\text{max}} < 1.0$ ) and minimum ( $0.15 < \phi_{\text{min}} < 0.70$ ; see Figure 4). Fitting the spectra from both phase ranges with an absorbed PL model led to differing photon indices of  $\Gamma_{\text{max}} = 1.41 \pm 0.04$  and  $\Gamma_{\text{min}} = 1.58 \pm 0.05$  for the pulse maximum and minimum, respectively. However, in these fits we have again neglected the contribution from the PWN, which is not resolved by NuSTAR and which has a similar 2–10 keV flux to the pulsar (see Section 3.2.2).

We account for the PWN emission for both phase ranges in the same way as discussed in Section 3.2.2. The resulting fitted values for the photon indices were  $\Gamma_{\text{max}} = 1.11 \pm 0.05$  ( $\chi^2_{85} = 0.91$ ) and  $\Gamma_{\text{min}} = 1.18 \pm 0.07$  ( $\chi^2_{70} = 0.84$ ). These results suggest that we cannot measure the difference between pulse maximum and pulse minimum when accounting for the PWN emission. The 3–79 keV unabsorbed fluxes for the pulse maximum and minimum (after accounting for the PWN emission) are  $F_{\text{max}} = (6.8 \pm 0.5) \times 10^{-12}$  erg cm<sup>-2</sup> s<sup>-1</sup> and  $F_{\text{min}} = (3.8 \pm 0.4) \times 10^{-12}$  erg cm<sup>-2</sup> s<sup>-1</sup>, respectively.

### 3.3. Source A = 2CXO J110158.4–605649: A Possible Counterpart to 4FGL J1102.0–6054

A serendipitously detected field point source, “Source A,” is also visible in the NuSTAR image at approximately R.A., decl. = 11:01:57.5, −60:56:58.3 (see Figure 1). SIMBAD lists two entries within 15'' of Source A’s position: the X-ray source

**Table 4**  
Misaligned Outflow Chandra Spectra

Segment	Area	Net Counts	$\Gamma$	$\mathcal{N}_{-5}$	$\chi^2_\nu$ (dof)	$F_{-13}$	$L_{33}$
1	9650	$4629 \pm 92$	$1.71 \pm 0.04$	$7.4 \pm 0.4$	1.12 (185)	$2.6 \pm 0.1$	$2.4 \pm 0.1$
2	9660	$4146 \pm 90$	$1.86 \pm 0.05$	$8.5 \pm 0.4$	0.99 (174)	$2.4 \pm 0.1$	$2.5 \pm 0.1$
3	33,180	$5803 \pm 157$	$1.74 \pm 0.05$	$12.7 \pm 0.6$	1.02 (389)	$4.2 \pm 0.1$	$4.0 \pm 0.1$

**Note.** Spectral fit results for the misaligned outflow using Chandra data (0.5–8 keV). Listed are the segment number, area (in arcsec<sup>2</sup>), net counts, photon index  $\Gamma$ , PL normalization (in units of  $10^{-5}$  photons s<sup>-1</sup> cm<sup>-2</sup> keV<sup>-1</sup> at 1 keV), reduced  $\chi^2_\nu$  ( $\nu$  degrees of freedom), observed (absorbed) 0.5–8 keV flux (in units of  $10^{-13}$  erg cm<sup>-2</sup> s<sup>-1</sup>), and luminosity (in units of  $10^{33}$  erg s<sup>-1</sup>, assuming  $d = 7$  kpc). In all fits, we set  $N_{\text{H}} = 0.99 \times 10^{22}$  cm<sup>-2</sup>.

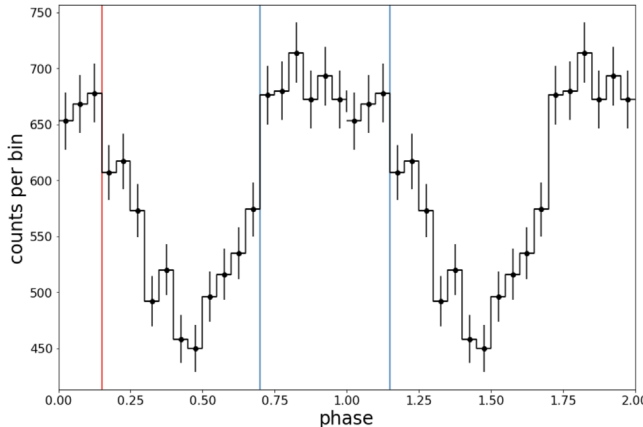


**Figure 4.** J1101 pulse profile in the 3–40 keV energy range. The red line shows the start of the phase range used for pulse minimum, which extends to the first blue line. Beyond the first blue line (at  $\phi = 0.70$ ) up until the second blue line corresponds to the phase range used for pulse maximum.

2XMM J110158.5–605651 (which is the bright source seen at Source A’s position in the CXO image; Figure 1 right panel), and the radio source RJJ2006 F (Reynoso et al. 2006). These two sources are positionally consistent with each other (within 5'') and with 2CXO J110158.4–605649 (R.A., decl. = 11:01:58.46, 60:56:49.91;  $\pm 0.^{\circ}74$ , 95% CL) and are thus likely counterparts to the same object as well as NuSTAR Source A. For RJJ2006 F, Reynoso et al. (2006) list a radio spectral index  $\alpha = 0.5 \pm 0.1$ , a 20 cm spectral flux density  $S = 57$  mJy (where  $S \propto \nu^\alpha$ ), a systemic velocity  $> 80$  km s<sup>-1</sup> (measured from its H I emission), and a kinematic distance  $> 14$  kpc. There is a Gaia source (source ID 5337957089788123136; parallax distance  $d = 4.34$  kpc) located 1''.95 from the Chandra position, though given its positional offset and its Galactic nature (in contrast to the likely extragalactic nature of Source A; see below), it is likely unrelated.

To find the  $N_{\text{H}}$  of Source A (=2CXO J110158.4–605649), we first fitted the Chandra data and found that its spectrum can be described by an absorbed PL model with  $N_{\text{H}} = (4.46 \pm 0.67) \times 10^{22}$  cm<sup>-2</sup>,  $\Gamma = 1.43 \pm 0.20$ ,  $\mathcal{N} = (5.1 \pm 1.7) \times 10^{-5}$  photon s<sup>-1</sup> cm<sup>-2</sup> keV<sup>-1</sup> (at 1 keV), and  $\chi^2_{119} = 0.92$ . The best-fit  $N_{\text{H}}$  value is well in excess of the maximum Galactic  $N_{\text{H}}$ : HEASARC’s  $N_{\text{H}}$  tool<sup>8</sup> lists the maximum Galactic  $N_{\text{H}}$  in the vicinity ( $r < 5'$ ) of Source A as being in the range of  $N_{\text{H}} = (1.17\text{--}1.26) \times 10^{22}$  cm<sup>-2</sup>.

Next, we fitted the NuSTAR data (independently from the Chandra data) with both models, and set  $N_{\text{H}}$  to the best-fit values (as found by Chandra) for each model. Both models provided satisfactory fits, with best-fit parameters consistent with those

found by Chandra. For the absorbed PL model, the NuSTAR data yielded  $\Gamma = 1.70 \pm 0.10$ ,  $\mathcal{N} = (10.5 \pm 2.3) \times 10^{-5}$  photons s<sup>-1</sup> cm<sup>-2</sup> keV<sup>-1</sup> at 1 keV, and  $\chi^2_{209} = 0.98$ . Considering Source A = 2CXO J110158.4–605649’s extragalactic nature implied by its  $N_{\text{H}}$  and H I emission, we propose that it is an AGN.

Our NuSTAR pointing also serendipitously covered the 95% error ellipse of 4FGL J1102.0–6054 (as well as the archival Chandra observations; see Figure 5). 4FGL J1102.0–6054 is classified (based on its spectral properties) as a blazar candidate of uncertain type (BCU) in the Second Data Release (DR2) of the Fourth Fermi-LAT Catalog (Ballet et al. 2020; the source was not listed as having its classification updated in DR3; Abdollahi et al. 2022). In Figure 6, we plot the spectral characteristics of the four most populous 4FGL classes of identified 4FGL sources (which account for 89.2% of identified sources), and 4FGL J1102. 4FGL’s hardness ratios, variability index, and PL index appear compatible with the range of those exhibited by flat-spectrum radio quasars (FSRQs). Thus, with Source A’s extragalactic nature (implied by its radio properties and X-ray spectrum), with its PL spectrum being compatible with AGN emission, and with the absence of any other bright hard X-ray sources in the vicinity, we propose an association with 4FGL J1102 and support its classification as a blazar (FSRQ).

## 4. Discussion

### 4.1. Misaligned Outflow

#### 4.1.1. Small-scale Structure

To investigate the misaligned outflow’s small-scale morphological features, we reanalyzed the high-resolution Chandra data. In Figure 7, we present the merged Chandra image binned by a factor of 0.5 to show subarcsecond features. There appears to be a region of faint emission that extends for  $\approx 2''\text{--}3''$  ahead of the pulsar (shown by the green arrow in the left panel of Figure 7). This distance significantly exceeds a plausible projected bow shock standoff distance,  $\theta_s \approx 0.^{\circ}34(\mu/15 \text{ mas yr}^{-1})n_{\text{H}}^{-1/2}(d/7 \text{ kpc})^{-2} \sin i$ , where  $\mu$  is the pulsar’s proper motion,  $n_{\text{H}}$  is the number density of the ambient medium (in units of cm<sup>-3</sup>), and  $i$  is the inclination angle of the pulsar’s velocity with respect to the line of sight (see, e.g., Brownsberger & Romani 2014). The enhancement of brightness slightly ahead of the pulsar can be explained by the escape of particles (likely facilitated by magnetic reconnection; further explained below) into the region of the draped and compressed magnetic field, illustrated by the inset in Figure 7.

Figure 7 (left panel) also shows two narrow streams originating from the pulsar region (marked by the cyan

<sup>8</sup> <https://heasarc.gsfc.nasa.gov/cgi-bin/Tools/w3nh/w3nh.pl>

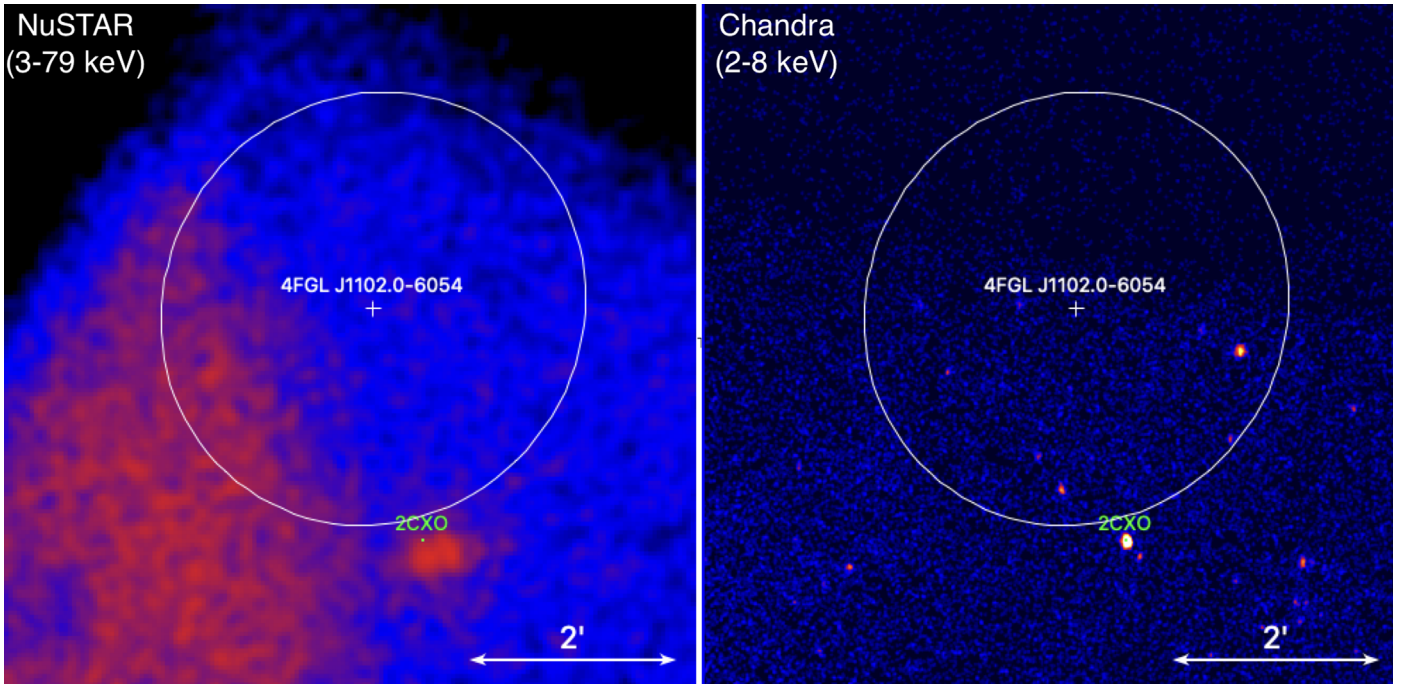


**Figure 5.** NuSTAR and Chandra images of the vicinity of 4FGL J1102.0-6054 (95% error ellipse is shown). Also shown is Source A = 2CXO J110158.4-605649 (abbreviated as “2CXO”). The Chandra image was restricted to the 2–8 keV range in an attempt to filter out possible thermal emission from nearby stars (i.e., sources unrelated to 4FGL J1102).

arrows). These streams may originate in opposite halves of the bow shock (see Olmi & Bucciantini 2019a; Barkov et al. 2019 for a discussion). These streams, clearly visible in the 0.5–5 keV range, are composed of particles that escape the bow shock apex region (which is unresolved from the pulsar in the X-ray images). We note that the pulsar wind particle escape requirement of having the gyroradius exceeding the bow shock standoff distance,  $r_g \gtrsim r_s = \theta_s d / \sin i$  (originally proposed by Bandiera (2008) for the Guitar PWN), translates into a rather stringent upper limit on the post-shock magnetic field  $B \lesssim 5(\mu/15 \text{ mas yr}^{-1})^{2/3}(d/7 \text{ kpc})^{2/3}(E/1 \text{ keV})^{1/3}n_H^{1/3} \mu\text{G}$ , where  $E$  is the synchrotron photon energy. Given that this field cannot be lower than the ISM field,  $B \gtrsim B_{\text{ISM}} \sim 5 \mu\text{G}$  (Ferrière 2015), the synchrotron emission can only be expected above  $E_c \sim 1(B_{\text{ISM}}/5 \mu\text{G})^3(\mu/15 \text{ mas yr}^{-1})^2(d/7 \text{ kpc})^{-2}n_H^{-1} \text{ keV}$ , because particles emitting synchrotron radiation at lower energies should not be escaping, as per the above requirement. Sensitive observations at IR frequencies can therefore test the Bandiera (2008) escape condition and place constraints on  $B_{\text{ISM}}$ ,  $n_H$ , and the distance to the pulsar. If the outflow is detected at frequencies far below those of X-rays (e.g., IR), it may imply that the particles in the outflow are ISM particles accelerated in the forward shock region (Bykov et al. 2017).

Particle escape can also be facilitated by magnetic reconnection of the external (ISM) magnetic field with the PWN’s magnetic field (Barkov et al. 2019). This is supported by the asymmetry of the outflow (i.e., the outflow not having a comparable counterpart on the opposite side of the PWN) because, in the magnetic reconnection scenario, the reconnection leads to particle acceleration and escape on the side of the PWN where the PWN magnetic field is directed opposite the ISM magnetic field (see Figure 5 of de Vries & Romani 2022 for an illustrative diagram). In the context of this scenario, we note that it is puzzling why the two arcsecond-scale mini-jets

(shown in the left panel of Figure 7) appear to be similar in brightness and size while the western outflow becomes far more prominent than the eastern one on larger scales and at greater distances from the pulsar (see Figure 7, right panel).

The deep Chandra images also show that (on arcsecond scales) the brightest part of the outflow (i.e., near the pulsar) does not just stream out along a straight line from the pulsar. In the vicinity of the pulsar, the outflow initially bends back in the direction opposite of the pulsar’s motion (toward the northeast) but then sharply turns toward the northwest (see the dashed green curve in the right panel of Figure 7). This indicates the presence of magnetic “draping” (Lyutikov 2006; Dursi & Pfrommer 2008) of the ISM magnetic field lines around the PWN bow shock.

In Figure 8, we present an unbinned Chandra image (see Figure 1). The image suggests that at least the dimmer portion of the main outflow, which is seen about 1' northwest of the pulsar, may be composed of multiple thread-like structures that run nearly parallel to each other along the outflow (highlighted by the dashed cyan lines in Figure 8). The threads could form as a result of streaming instability (see, e.g., the X-ray “stripes” in the Tycho SNR forward shock; Bykov et al. 2011; see also Section 6.5 of Bykov et al. 2017). Alternatively, the threads may represent variations in PWN reconnection with the external (ISM) magnetic field, sampled as the pulsar travels through an inhomogeneous ISM. The variations in reconnection can be due to variations of the external medium density, field geometry, and/or instabilities in the PWN flow. For example, the bubble structures seen in  $H_{\alpha}$  images of the Guitar PWN (PSR B2224+65; see Figure 2 of Chatterjee & Cordes 2002) indicate that the ISM density can substantially vary on scales as small as  $\sim 20''$  ( $2.5 \times 10^{17} \text{ cm}$  at  $d = 0.8 \text{ kpc}$ ; see Yoon & Heinz 2017). The density variations would change the ratio of shock standoff distance to pulsar

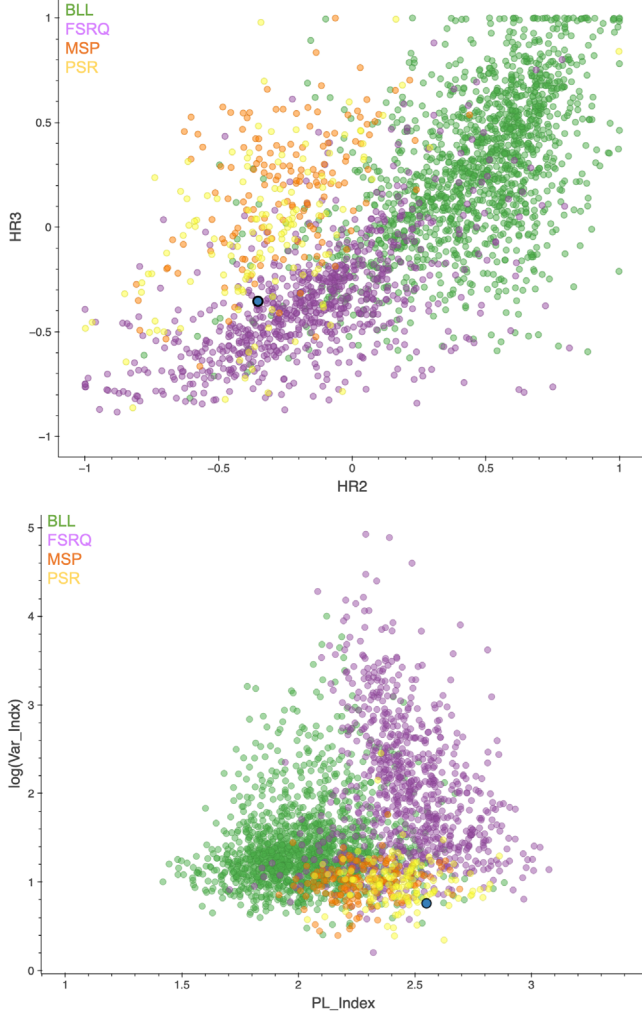


**Figure 6.** Plots of 4FGL-DR3 sources in different phase spaces. Shown are the most populous source classes (besides unidentified sources): BL Lac objects (BLL; green), flat-spectrum radio quasars (FSRQs; magenta), millisecond pulsars (MSPs; orange), and pulsars (PSRs; yellow); the blue bolded point marks 4FGL J1102.0-6054. Top: Hardness ratios HR2 vs. HR3 (where  $HR2 = (F7+F6+F5+F4)/(F7+F6+F5+F4)$ ,  $HR3 = (F6+F5+F4-F2-F3)/(F6+F5+F4+F2+F3)$ , and  $F\#$  are the fluxes in different Fermi-LAT energy bands as defined in 4FGL-DR3. Bottom: Log of the variability index vs. the PL index. Plots were produced by GCLASS: <https://home.gwu.edu/~kargaltsev/GCLASS>.

wind particle gyroradius, thus modulating the escape rate of particles (de Vries & Romani 2022). At the Lighthouse PWN’s distance  $d = 7$  kpc, such length scales correspond to  $\approx 2''.5$ , which is comparable to the  $\approx 6''$ – $8''$  separation of the thread-like structures shown in Figure 8. It is also interesting that the threads are most prominent in the dimmer region of the outflow (about  $1'$  from the pulsar) and that the outflow returns to roughly its initial brightness shortly after (about  $2'$  from the pulsar). This suggests that the flow speed and/or magnetic field strength may vary substantially on parsec-scale distances along the outflow.

Another notable feature of the outflow is that it seems to originate not only from the bow shock apex but also from the tail. This implies that the particles are leaking out of both the tail and the bow shock apex (as appears to be the case in the simulations of Olmi & Bucciantini (2019c)—see their Figure 5).

#### 4.1.2. Energetics, Flow Properties, and Magnetic Field

The NuSTAR detection of the Lighthouse PWN marks the first detection of a misaligned outflow in the hard X-ray band (above  $\sim 10$  keV). In the 136 ks NuSTAR exposure, the outflow is clearly seen up to  $\sim 25$  keV, with the far reaches of it (segment 3) possibly being detected above 50 keV (though this may be unrelated background emission, as suggested by the poorer quality fit to this segment compared to the other two). The outflow’s overall shape and size appear the same in both the NuSTAR and Chandra images, indicating that they do not exhibit a strong dependence on energy, at least up to  $\sim 25$  keV (i.e., the highest energy at which all segments are seen), which implies that the electrons emitting at higher energies do not lose most of their energy by the time they reach the farthest discernible part of the outflow (i.e., the synchrotron cooling is weak or moderate).

The strongly elongated shape of the outflow suggests that the magnetic field is predominantly oriented along the outflow, making it easier for particles to travel in that direction. Because the shape and size of segment 3 of the outflow appear to be the same in the Chandra and NuSTAR images, the particle travel time along the outflow,  $t_{\text{trav}}$ , must be smaller<sup>9</sup> than the synchrotron cooling time,  $t_{\text{syn}} \sim 1000(E_{\text{syn}}/25 \text{ keV})^{-1/2}(B/5 \mu\text{G})^{-3/2} \text{ yr}$ .

From the Chandra data, we can estimate the X-ray efficiency in the 0.5–8 keV band.<sup>10</sup> With the tail’s luminosity  $L_{0.5-8 \text{ keV}} = 7.4 \times 10^{33} \text{ erg s}^{-1}$ , its efficiency is similar,  $\eta_X = 5.3 \times 10^{-3}$ . Thus, the PWN’s total X-ray efficiency  $\eta_X = 1.2 \times 10^{-2}$ . We note that the X-ray efficiencies of other prominent misaligned outflows, associated with PSRs B2224+65, J1509-5850, and J2030+4415, are  $8 \times 10^{-4}$  ( $d = 0.83$  kpc),  $8 \times 10^{-4}$  ( $d = 3.8$  kpc), and  $2 \times 10^{-4}$  ( $d = 0.5$  kpc), respectively, i.e., significantly lower. The J1101 outflow’s 3–79 keV efficiency is  $\eta_X = 1.4 \times 10^{-2}$ .

Using the spectra and fluxes of the misaligned outflow measured in several segments, we can crudely estimate magnetic fields in those regions. For a PL synchrotron spectrum with photon index  $\Gamma$ , the magnetic field at a given magnetization parameter  $\sigma = w_B/w_e$  (the ratio of magnetic to particle kinetic energy densities) depends on the ratio of the luminosity  $L(\nu_m, \nu_M)$  measured in the  $\nu_m < \nu < \nu_M$  frequency range (here,  $h\nu_m = 0.5$  keV and  $h\nu_M = 25$ ), to the radiating volume  $V$  (see, e.g., Klingler et al. 2016a):

$$B = \left[ \frac{L(\nu_m, \nu_M)\sigma}{\mathcal{A}V} \frac{\Gamma - 2}{\Gamma - 1.5} \frac{\nu_1^{1.5-\Gamma} - \nu_2^{1.5-\Gamma}}{\nu_m^{2-\Gamma} - \nu_M^{2-\Gamma}} \right]^{2/7}. \quad (1)$$

In this equation,  $\nu_1$  and  $\nu_2$  are the characteristic synchrotron frequencies ( $\nu_{\text{syn}} \approx 3eB\gamma^2/4\pi mc$ ) corresponding to the boundary energies ( $\gamma_1 m_e c^2$  and  $\gamma_2 m_e c^2$ ) of the electron spectrum ( $dN_e/d\gamma \propto \gamma^{-p} \propto \gamma^{-2\Gamma+1}$ ;  $\gamma_1 < \gamma < \gamma_2$ ), and  $\mathcal{A} = 2^{1/2}e^{7/2}/(18\pi^{1/2}m_e^{5/2}c^{9/2})$ . For each misaligned outflow segment, we take the average of the  $\Gamma$  and normalization as measured by Chandra and NuSTAR (listed in Tables 3 and 4),

<sup>9</sup> We note that the following estimate is applicable only if the particle motion across the magnetic field lines is relativistic and the gyroradii are small compared to the outflow spatial scales. The estimate is inapplicable if the particles simply stream along the magnetic field lines (i.e., if their motion is parallel to magnetic field lines, in which case they would not be emitting synchrotron radiation).

<sup>10</sup> We use this energy range because it allows for comparison with other misaligned outflows, as currently only the Lighthouse PWN has been studied in the hard X-ray band.

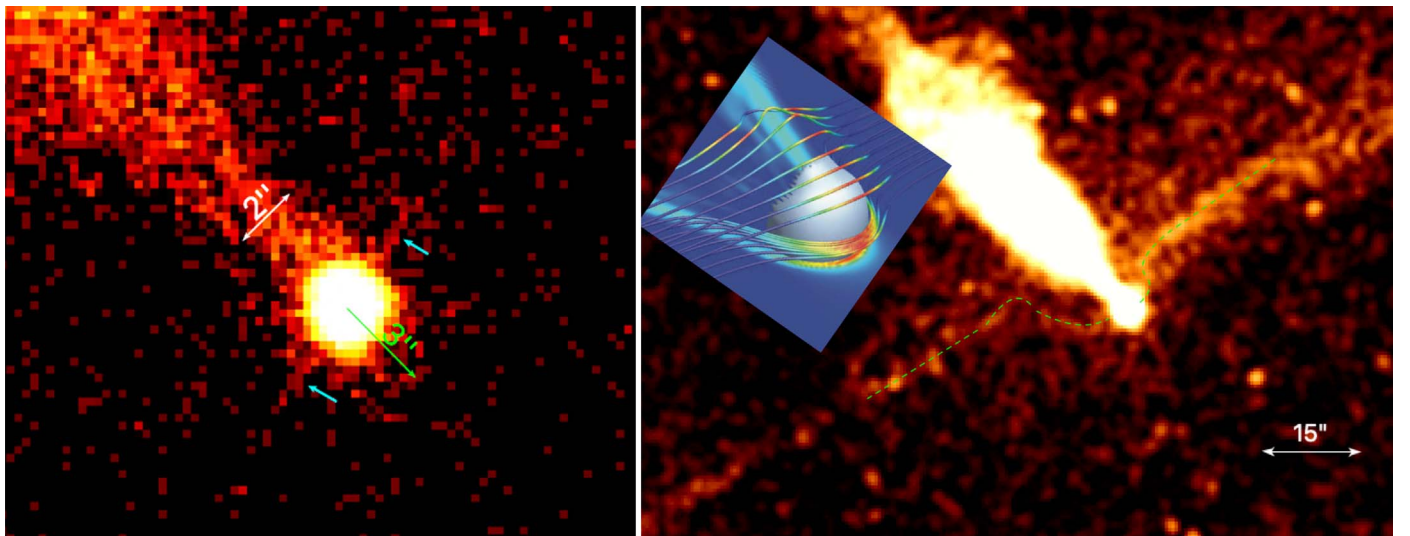


**Figure 7.** Chandra images showing the fine structure in the vicinity of the Lighthouse PWN bow shock. Left: Zoomed-in image of the pulsar (binned by a factor of 0.5 to show subarcsecond features) showing hints of narrow streams originating from the pulsar (marked by cyan arrows), and enhanced emission seen up to 3'' ahead of the pulsar (shown by the green arrow). Right: Zoomed-out image showing evidence of “magnetic draping” of the ISM magnetic field lines around the PWN bow shock (marked by the green dashed curves). The inset image is an illustration of magnetic draping from Dursi & Pfrommer (2008).

and we calculate the 0.5–25 keV luminosities using those averaged values. The NuSTAR analysis regions used in the above spectral analyses are wider than the actual width of the outflow, due to its large PSF, so we use the higher-resolution Chandra images to estimate the volume. We approximate segments 1 and 2 as cylinders of radius  $r = 30''$  and length  $l = 100''$ . We approximate segment 3 as a sphere of radius  $r = 100''$ . Because  $L \propto d^2$  and  $V \propto d^3$ , the magnetic field estimated from Equation (1) weakly depends on the assumed distance,  $B \propto d^{-2/7}$ . The exact value of  $\nu_2$  is not really important as long as  $(\nu_1/\nu_2)^{1-1.5} \ll 1$ , so we choose a plausible value  $h\nu_2 = 25$  keV. We assume  $h\nu_1 = 0.5$  keV: the lowest energy at which the outflow has been observed. It is possible that the actual  $h\nu_1$  is lower, but it cannot be determined with the currently available data.

For segments 1–3, we estimated  $B_1 \sim 6 \sigma^{2/7} \mu\text{G}$ ,  $B_2 \sim 6 \sigma^{2/7} \mu\text{G}$ , and  $B_3 \sim 4 \sigma^{2/7} \mu\text{G}$ . The unknown lower boundary frequency  $\nu_1$  is the main source of uncertainty of the magnetic field estimates for the measured spectral slopes. In reality,  $h\nu_1$  may be lower than 0.5 keV, in which case the estimated magnetic field will be higher. Thus, the above estimates should be considered lower limits. For example, if we set  $h\nu_1 = 1$  eV, the magnetic field estimates change to  $\sim 10$ ,  $\sim 14$ , and  $\sim 10 \sigma^{2/7} \mu\text{G}$ , respectively. Also, there may be a spectral break below the lower observed frequency or lower boundary frequency, which is another reason to interpret these estimates as crude lower limits. Finally, we note that the magnetic field estimate for segment 3 may not be as accurate as that estimated for the other segments, because it is likely that segment 3 is not a spherical structure (as we approximated) but rather is composed of more compact filamentary structures. However, the existing Chandra data do not allow us to reliably estimate the precise morphology (and volume) of this segment of the tail; hence our spherical approximation.

One can estimate the Lorentz factors of the escaped particles as  $\gamma \sim 3 \times 10^8 (E_{\text{syn}}/8 \text{ keV})^{1/2} (B/5 \mu\text{G})^{-1/2}$ , corresponding to  $\gamma = (1-5) \times 10^8$  range for the 1–25 keV energies of the observed synchrotron photons. The upper value is a factor of 10

below the maximum  $e^-/e^+$  Lorentz factor  $\gamma_{\max} = 4.8 \times 10^9$  ( $\approx 2.4$  PeV) corresponding to the theoretical maximum accelerating potential between the pulsar’s pole and light cylinder,  $\Delta\Phi = (3\dot{E}/2c)^{1/2}$  (Goldreich & Julian 1969). We note that the Guitar Nebula’s pulsar, B2224+65, has much lower  $\dot{E} = 1.2 \times 10^{33} \text{ erg s}^{-1}$ , resulting in  $\gamma_{\max} = 1.4 \times 10^8$ , which is somewhat below  $\gamma \sim 3 \times 10^8 (E_{\text{syn}}/8 \text{ keV})^{1/2} (B/5 \mu\text{G})^{-1/2}$  for the highest-energy photons observed in the misaligned outflow of the Guitar nebula. This lends support to the possibility that particles populating misaligned outflows may be ISM particles accelerated between the forward shock and pulsar wind termination shock ahead of the moving pulsar (see Bykov et al. 2017). In this case, the one-sidedness of the outflows may be explained by the fact that electrons and positrons would drift in opposite directions in an ordered magnetic field, and there are more electrons than positrons in the ISM ahead of the pulsar.

#### 4.1.3. Comparison with Other Misaligned Outflows

While all known misaligned pulsar outflows exhibit remarkably similar spectra in the 0.5–8 keV band ( $\Gamma = 1.6$ –1.7), they can exhibit different morphologies. For example, the width of the Lighthouse outflow appears to increase nearly linearly with distance from the pulsar up to about 4'.5 (9 pc), after which point the outflow suddenly widens, while a central (bright) part of the outflow appears to “wiggle.” Conversely, its smaller counter-outflow appears to narrow with distance. If the conical contours of the main outflow (shown by the dashed lines in left panel of Figure 9) are continued through the PWN tail, it would appear to match the contours of the shorter counter-outflow. If this is the case, it could mean that the outflow and counter-outflow are just two regions (sides) of the same structure.

Linear expansion with distance from the pulsar is also clearly seen in the PSR J1509–5850 misaligned outflow ( $d_{\text{DM}} \sim 3.8$  kpc;  $160 < v_{\perp,\text{psr}} < 640 \text{ km s}^{-1}$ ; see Figure 9 and Klingler et al. 2016a), but the rapid sideways expansion at the end is not seen (though it is not clear whether the J1509

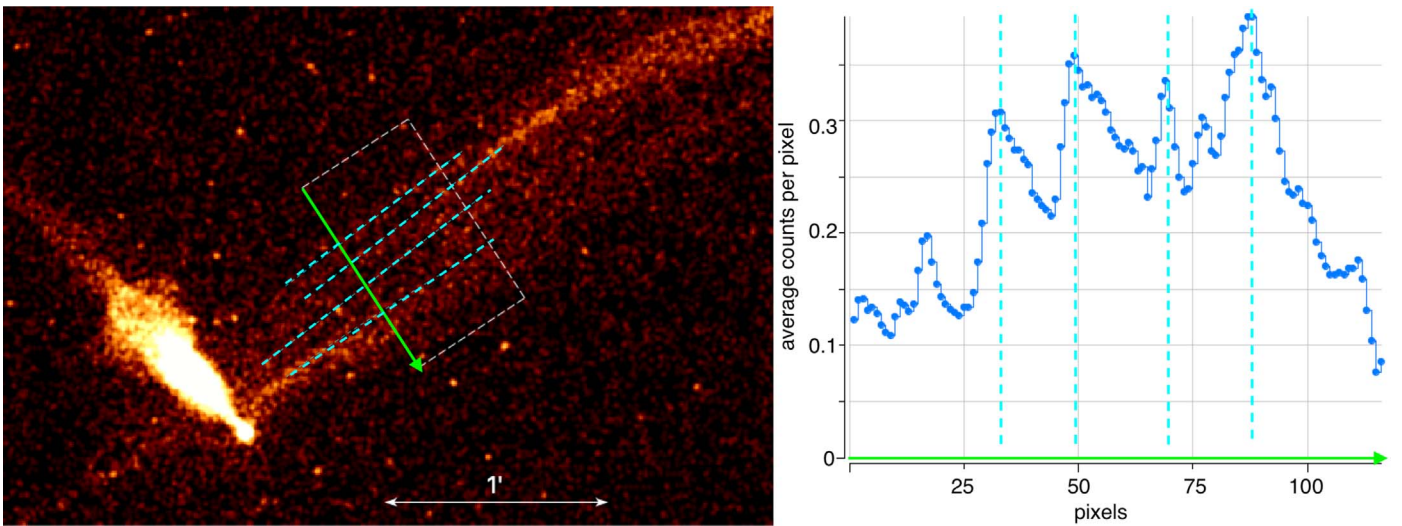


**Figure 8.** Left: Merged unbinned Chandra image (286 ks, smoothed with a  $r = 3$  pixel ( $1.5''$ ) Gaussian kernel) showing the thread-like fine structure of the dimmer section of the misaligned outflow. The dashed green box represents the area used to produce the brightness profile in the right panel. Right: Brightness profile of the portion of the outflow enclosed by the dashed white box. The profile is taken in the transverse direction, which is shown by the green arrow. The thin dashed cyan lines are used to highlight the apparent thread-like substructures. One Chandra-ACIS pixel corresponds to  $0.492''$ .

outflow indeed lacks this behavior, or if it does expand outside the ACIS field of view), and no central (bright) interior is seen. Unlike the Lighthouse outflow, the J1509 and Guitar outflows do not exhibit thread-like substructures. It is not that they cannot be resolved, as the J1509 and Guitar PWNe lie at roughly half and one-tenth (respectively) the distances of the Lighthouse PWN. Unlike the J1509 and Lighthouse outflows, the Guitar outflow ( $d = 0.83 \pm 0.14$  kpc;  $v_{\perp,\text{psr}} = 770 \pm 130$  km s $^{-1}$ ; Deller et al. 2019) first widens with distance from the pulsar but then become slightly narrower (Figure 9). Also, the Guitar PWN, which was so named because of its guitar-shaped H- $\alpha$  tail (Chatterjee & Cordes 2002; Brownsberger & Romani 2014; de Vries & Romani 2022), lacks an X-ray tail. This could be due to the lower spin-down power,  $\dot{E} = 1.2 \times 10^{33}$  erg s $^{-1}$ , and therefore a lower accelerating potential of the Guitar pulsar, such that the pulsar wind particles in the tail are not energetic enough to emit X-rays. If this is the case, it would mean that the particle leakage mechanism (i.e., reconnection of the PWN and ISM magnetic fields) is substantially accelerating the pulsar wind, or that the particles are additionally accelerated in the transrelativistic colliding flows (between the forward shock and termination shock of the pulsar wind) ahead of the pulsar, from where they leak to the ISM (Bykov et al. 2017).

Further observations of these magnificent structures are needed to elucidate the reasons for these contrasting behaviors and to further our understanding of the complex interactions between pulsar winds and the ISM magnetic field.

#### 4.2. Pulsar

The NuSTAR pulse profile of J1101 shows a single broad peak with a relatively flat top that spans about half of the phase interval. This is similar to the pulse profiles found with XMM-Newton in the 0.5–10 keV band by Halpern et al. (2014) and with NICER in the 1.5–10 keV band by Ho et al. (2022). The pulsation period detected with NuSTAR is consistent with the ephemeris of Ho et al. (2022). We find no pulse profile dependence on energy up to at least 40 keV.

The spectra of the pulsar+PWN are generally in agreement with those found by Pavan et al. (2016). We also performed phase-resolved spectroscopy in two broad phase bins. However, due to a lack of statistics and the contaminating PWN, we do not find any statistically significant evidence of a changing photon index with phase, contrary to what has been observed in several other pulsars (e.g., Chen et al. 2016; Hare et al. 2021).

## 5. Conclusions

We have presented NuSTAR observations of PSR J1101–6101 and the Lighthouse PWN. The entire outflow is clearly seen up to  $\sim 25$  keV, and the distal segment of it is marginally seen up to  $\sim 50$  keV (though the statistics are insufficient to discern whether it is unrelated background emission or synchrotron emission from the distal segment of the outflow). The outflow’s shape and  $7'$  (14 pc) extent as seen in the 20–25 keV band (and lower energies) are consistent with those seen in the 0.5–8 keV band by Chandra (though the outflow’s true extent may be limited by the FOV of both observatories). We found marginal evidence of synchrotron cooling along the outflow, with the spectral slope increasing from  $\Gamma \approx 1.8 \pm 0.1$  to  $\Gamma \approx 2.2 \pm 0.1$  in the NuSTAR band. We crudely estimated an equipartition outflow magnetic field strength for the outflow,  $B \gtrsim (4\text{--}6) \mu\text{G}$ , which is comparable to the ISM magnetic field.

We reanalyzed archival high-resolution Chandra images of the Lighthouse PWN misaligned outflow to investigate its arcsecond-scale structure. We found evidence that at least part of the outflow is composed of multiple thread-like structures that run nearly parallel to each other, which may form from Weibel or Bell streaming instability—or more likely, from variations in PWN-ISM magnetic field reconnection. The Chandra images show that part of the outflow appears to originate from the pulsar tail rather than from the immediate vicinity of the pulsar, which may indicate that particles are leaking out of not just the bow shock apex but the pulsar tail as well. We also found that the outflow bends around the bow shock apex, indicating the presence of magnetic “draping” of the ISM magnetic field lines around the PWN bow shock.

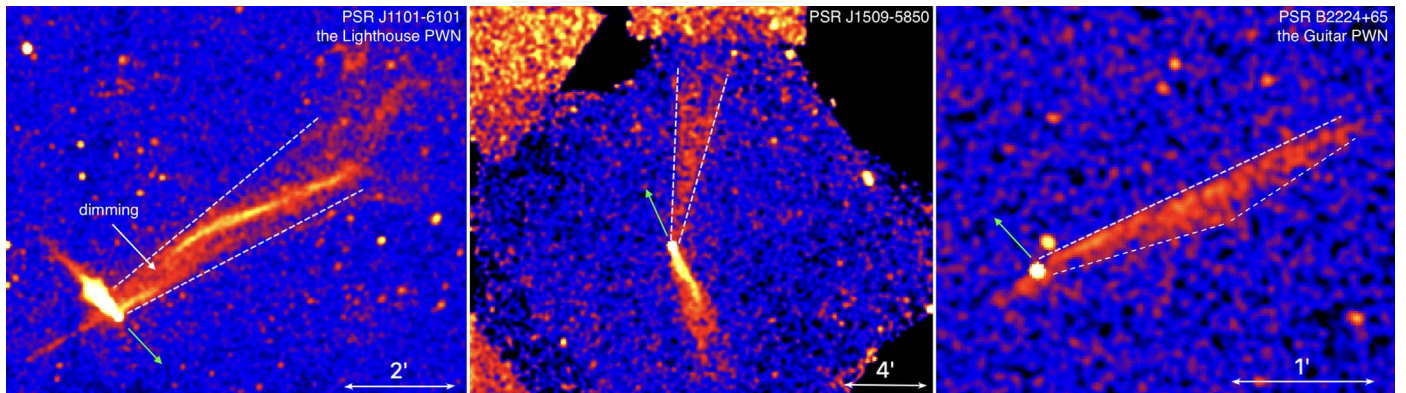


**Figure 9.** Chandra images of the misaligned outflows produced by pulsars J1101–6101 (the Lighthouse PWN), J1509–5850, and B2224+65 (the Guitar PWN). The dashed lines in the left and middle panels show the linear widening with distance seen in the Lighthouse and J1509 PWNe; the dashed line in the right panel shows the leading edge of the Guitar PWN outflow. The green arrows mark the pulsars’ directions of motion.

We have performed NuSTAR timing analysis on PSR J1101–6101. We found pulsations up to 40 keV at the frequency found by Ho et al. (2022) from recent NICER data, and presented the pulse profile. The consistency with the archival ephemeris suggests that this pulsar does not glitch frequently.

With NuSTAR, we also detected the serendipitous X-ray source 2CXO J110158.4–605649. We propose that it is the counterpart to the gamma-ray source 4FGL J1102.0–6054, and we present evidence that supports its classification as a flat-spectrum radio quasar.

### Acknowledgments

The authors wish to thank Karl Forster for assistance in planning the NuSTAR observations, and Andrei Bykov for useful discussions. Support for this work was provided by the National Aeronautics and Space Administration through the NuSTAR award 80NSSC21K0055. N.K. acknowledges support provided by NASA under award number 80GSFC21M0002. J.H. acknowledges support from an appointment to the NASA Postdoctoral Program at the Goddard Space Flight Center, administered by the ORAU through a contract with NASA. O.K. acknowledges support provided by NASA through Chandra Award Number G01-22055B issued by the Chandra X-ray Center, which is operated by the Smithsonian Astrophysical Observatory for and on behalf of NASA under contract NAS8-03060.

**Software:** HEASoft (NASA High Energy Astrophysics Science Archive Research Center (Heasarc), 2014), CIAO (Fruscione et al. 2006), Fermipy (Wood et al. 2017), Fermitoools (NASA High Energy Astrophysics Science Archive Research Center (Heasarc), 2014).

### ORCID iDs

Noel Klingler <https://orcid.org/0000-0002-7465-0941>  
 Jeremy Hare <https://orcid.org/0000-0002-8548-482X>  
 Oleg Kargaltsev <https://orcid.org/0000-0002-6447-4251>  
 George G. Pavlov <https://orcid.org/0000-0002-7481-5259>  
 John Tomsick <https://orcid.org/0000-0001-5506-9855>

### References

- Abdollahi, S., Acero, F., Baldini, L., et al. 2022, *ApJS*, 260, 53  
 Bachetti, M., Markwardt, C. B., Grefenstette, B. W., et al. 2021, *ApJ*, 908, 184
- Ballet, J., Burnett, T. H., Digel, S. W., et al. 2020, arXiv:2005.11208  
 Bandiera, R. 2008, *A&A*, 490, L3  
 Barkov, M. V., & Lyutikov, M. 2019, *MNRAS Lett.*, 489, L28  
 Barkov, M. V., Lyutikov, M., Klingler, N., et al. 2019, *MNRAS*, 485, 2041  
 Brownsberger, S., & Romani, R. W. 2014, *ApJ*, 784, 154  
 Buccieri, R., Bennett, K., Bignami, G. F., et al. 1983, *A&A*, 128, 245  
 Bykov, A. M., Amato, E., Petrov, A. E., et al. 2017, *SSRV*, 207, 235  
 Bykov, A. M., Ellison, D. C., Osipov, S. M., et al. 2011, *ApJL*, 735, L40  
 Chatterjee, S., & Cordes, J. M. 2002, *ApJ*, 575, 407  
 Chen, G., An, H., Kaspi, V. M., et al. 2016, *ApJ*, 817, 93  
 de Vries, M., & Romani, R. W. 2020, *ApJL*, 896, L7  
 de Vries, M., & Romani, R. W. 2022, *ApJ*, 928, 39  
 Deller, A. T., Goss, W. M., Brisken, W. F., et al. 2019, *ApJ*, 875, 100  
 Dursi, L. J., & Pfrommer, C. 2008, *ApJ*, 677, 993  
 Ferrière, K. 2015, *JPhCS*, 577, 012008  
 Fruscione, A., McDowell, J. C., Allen, G. E., et al. 2006, *Proc. SPIE*, 6270, 62701V  
 García, F., Combi, J. A., Albacete-Colombo, J. F., et al. 2012, *A&A*, 546, A91  
 Goldreich, P., & Julian, W. H. 1969, *ApJ*, 157, 869  
 Halpern, J. P., Tomsick, J. A., Gotthelf, E. V., et al. 2014, *ApJL*, 795, L27  
 Hare, J., Volkov, I., Pavlov, G. G., et al. 2021, *ApJ*, 923, 249  
 Harrison, F. A., Craig, W. W., Christensen, F. E., et al. 2013, *ApJ*, 770, 103  
 Ho, W. C. G., Kuiper, L., Espinoza, C. M., et al. 2022, *ApJ*, 939, 7  
 Johnson, S. P., & Wang, Q. D. 2010, *MNRAS*, 408, 1216  
 Kargaltsev, O., Cerutti, B., Lyubarsky, Y., et al. 2015, *SSRV*, 191, 391  
 Kargaltsev, O., Pavlov, G. G., Klingler, N., et al. 2017, *JPhCS*, 83, 635830501  
 Klingler, N., Kargaltsev, O., Rangelov, B., et al. 2016a, *ApJ*, 828, 70  
 Klingler, N., Rangelov, B., Kargaltsev, O., et al. 2016b, *ApJ*, 833, 253  
 Klingler, N., Yang, H., Hare, J., et al. 2020, *ApJ*, 901, 157  
 Lyutikov, M. 2006, *MNRAS*, 373, 73  
 Madsen, K. K., Beardmore, A. P., Forster, K., et al. 2017, *AJ*, 153, 2  
 Madsen, K. K., Forster, K., Grefenstette, B. W., et al. 2022, *JATIS*, 8, 034003  
 Manchester, R. N., Hobbs, G. B., Teoh, A., & Hobbs, M. 2005, *AJ*, 129, 1993  
 Marelli, M., Pizzocaro, D., De Luca, A., et al. 2016, *ApJ*, 819, 40  
 Nasa High Energy Astrophysics Science Archive Research Center (Heasarc) 2014, HEASoft: Unified Release of FTOOLS and XANADU, Astrophysics Source Code Library, ascl:1408.004  
 Olmi, B., & Bucciantini, N. 2019a, *MNRAS*, 484, 5755  
 Olmi, B., & Bucciantini, N. 2019b, *MNRAS*, 488, 5690  
 Olmi, B., & Bucciantini, N. 2019c, *MNRAS*, 490, 3608  
 Pavan, L., Bordas, P., Pühlhofer, G., et al. 2014, *A&A*, 562, A122  
 Pavan, L., Bozzo, E., Pühlhofer, G., et al. 2011, *A&A*, 533, A74  
 Pavan, L., Pühlhofer, G., Bordas, P., et al. 2016, *A&A*, 591, A91  
 Reynolds, S. P., Pavlov, G. G., Kargaltsev, O., et al. 2017, *SSRV*, 207, 175  
 Reynoso, E. M., Johnston, S., Green, A. J., et al. 2006, *MNRAS*, 369, 416  
 Tomsick, J. A., Bodaghee, A., Rodriguez, J., et al. 2012, *ApJL*, 750, L39  
 Van Etten, A., Romani, R. W., & Ng, C.-Y. 2008, *ApJ*, 680, 1417  
 Verbunt, F., Igoshev, A., & Cator, E. 2017, *A&A*, 608, A57  
 Volkov, I., Kargaltsev, O., Younes, G., et al. 2021, *ApJ*, 915, 61  
 Wilms, J., Allen, A., & McCray, R. 2000, *ApJ*, 542, 914  
 Wood, M., Caputo, R., Charles, E., et al. 2017, *ICRC (Busan)*, 301, 824  
 Yoon, D., & Heinz, S. 2017, *MNRAS*, 464, 3297  
 Yusef-Zadeh, F., Wardle, M., Heinke, C., et al. 2021, *MNRAS*, 500, 3142  
 Zhang, S., Zhu, Z., Li, H., et al. 2020, *ApJ*, 893, 3